Available online at www.sciencedirect.com
SCIENCE DIRECT®
Physica D 194 (2004) 333–356
PHYSICA D
www.elsevier.com/locate/physd

Multimodal regimes in a compartmental model of the dopamine neuron

Georgi S. Medvedev [a,*], Jaime E. Cisternas [b]

[a] *Department of Mathematics, Drexel University, 3141 Chestnut Street, Philadelphia, PA 19104, USA*
[b] *Program in Applied and Computational Mathematics, Princeton University, Princeton, NJ 08544-1000, USA*

Received 27 August 2003; received in revised form 13 February 2004; accepted 16 February 2004
Communicated by J.P. Keener

Abstract

We study chains of strongly electrically coupled relaxation oscillators modeling dopamine neurons. When individual oscillators are in the regime close to an Andronov–Hopf bifurcation (AHB), the coupled system exhibits a variety of oscillatory behavior. We show that the proximity of individual oscillators to the AHB has a significant impact on the system dynamics in a wide range of parameters. It manifests itself through a family of stable multimodal periodic solutions that are composed out of large-amplitude relaxation oscillations and small-amplitude oscillations. This family of solutions has a rich bifurcation structure. The waveform and the period vary greatly across the family. The structure and bifurcations of the stable periodic solutions of the coupled system are investigated using numerical and analytic techniques.

PACS: 87.17.Nn

Keywords: Andronov–Hopf bifurcation; Chains of coupled oscillators; Multimodal oscillations

1. Introduction

Understanding the mechanisms responsible for generating various patterns of electrical activity (firing patterns) in individual neurons and neural networks is important for understanding of how nervous system encodes and processes information [10,49]. The transient changes in the rate of firing in dopamine neurons (DNs) in the mammalian brain stem have been suggested to act as an error prediction signal [51]. DNs exhibit three distinct firing patterns: rhythmic and irregular single spiking, and bursting. Experimental studies have shown that these modes of firing are determined by the intrinsic properties of the cells. Wilson and Callaway [52] proposed a coupled oscillator model to explain the origin of the rhythmic firing pattern and to shed light on the possible mechanisms for other firing patterns in DNs. The Wilson–Callaway model reproduces all the salient features of the rhythmic firing of DNs: synchronous oscillations of the membrane potential at different locations along the dendrite, calcium transients, and spike-frequency adaptation. The model can be described as a chain of two-dimensional relaxation oscillators with varying natural frequencies of

* Corresponding author. Fax: +1-215-8951582.
E-mail addresses: medvedev@drexel.edu (G.S. Medvedev), jcistern@princeton.edu (J.E. Cisternas).

0167-2789/$ – see front matter © 2004 Elsevier B.V. All rights reserved.
doi:10.1016/j.physd.2004.02.006

oscillations, which are strongly coupled via fast variables by diffusive coupling. The individual oscillators are in the regime close to a supercritical AHB [32]. The dynamics of an individual oscillator near an AHB can switch between the full-amplitude relaxation oscillations and small-amplitude (subthreshold) oscillations under small variation of parameters. The subthreshold oscillations occupy a small region in the parameter space of a single relaxation oscillator, which is followed by a sharp transition to full-amplitude relaxation oscillations. The situation is different for the coupled system. We show that in the Wilson–Callaway model, the AHB has a significant impact on the system dynamics in a wide region of parameters. It manifests itself through a family of stable multimodal periodic solutions that are composed out of large-amplitude relaxation oscillations and small-amplitude oscillations. This family of solutions has a rich bifurcation structure. The waveform and the period of these solutions vary greatly across the family. Therefore, proximity of individual oscillators to an AHB endows the coupled system with pattern-forming capacity. Our results suggest that the proximity of the intrinsic dynamics in individual compartments to an AHB is likely to result in the variability of behavior of the DNs and to play a role in the mechanisms for generating more complex firing patterns, such as irregular spiking and bursting. However, explaining the latter would require more detailed biophysical models. In the present paper, we focus on studying the effects of the proximity of individual oscillators to an AHB on the dynamics of the coupled system and on investigating the structure of the family of multimodal periodic solutions.

Mixed-mode oscillations have been observed in many chemical reactions, including famous Belousov–Zhabotinskii reaction (see [7,28,40,42,45,50] and references therein). Numerical studies of several prototypical models of autocatalytic reactions have revealed that the families of mixed-mode solutions possess complex bifurcation structure: the regions of periodic behavior (which frequently exhibit period-adding) alternate with period-doubling cascades and chaotic behavior [28,45]. Similar bifurcation scenarios were observed in the families of one-dimensional bimodal maps [12,46]. A geometric explanation of the mechanism responsible for the generation of mixed-mode oscillations in a model of an autocatalytic reaction was suggested in [40]. In [40], the canard trajectories [5,8,11,15], which separate the large-amplitude periodic orbits from the small-amplitude ones, were used to construct a Poincare map for the multimodal periodic orbits. The Poincare map, obtained numerically in [40], was shown to be bimodal. It accounted for the bifurcation sequences of the mixed-mode solutions. In the present paper, we show that a similar mechanism is responsible for generating the multimodal periodic solutions in the Wilson–Callaway model. In [52], the mixed-mode oscillations were reported in a large compartmental model (264 compartments). We show that the mechanism for generating mixed-mode oscillations does not require a large number of oscillators in the chain: systems of two coupled oscillators can produce multimodal solutions. For simplicity, we study a system of two coupled oscillators, for which we can give more a complete analysis. Our analysis extends the method developed in [38,39] to cover the case when the oscillators in the chain are close to an AHB. The key observation in [39] is that, in the limit of the strong coupling and under some assumptions on the coefficients, the system of N electrically coupled oscillators can be approximated by an integrable system. The latter has an $(N-1)$-parameter family of periodic orbits that forms a cylinder in the phase space. This allows one to use ideas similar to those of the method of averaging [6,20]. In particular, in the neighborhood of the cylinder foliated by the periodic orbits of the approximate system, we introduce a function, which measures the deviation of the trajectory from its initial position after one full cycle of oscillations. This function can be interpreted as a Lyapunov function, because it decays after each cycle of oscillations, and it is bounded from below. The Lyapunov function is used to locate the family of the mixed-mode limit cycles for the coupled system and to construct a Poincare map. The analysis of the family of the Poincare maps explains the structure of the family of multimodal solutions for the coupled system.

The outline of the paper is as follows. In Section 2, we present the results of the numerical analysis of the bifurcation structure of solutions of a system of two coupled oscillators. Using numerical continuation techniques, we show that the mixed-mode solutions typically lie on the closed curves (isolas) in the parameter space, and characterize the sequence, in which stable mixed-mode solutions appear as a control parameter is varied. In Section 3, we analyze

the system of two coupled oscillators. The main steps of the analysis are the reduction of the original problem to a set of two-dimensional problems and the derivation of the Poincare maps and their piecewise linear approximations for the reduced problems. We identify a 1D map that determines the dynamics of the coupled system and show that the most part of the bifurcation sequence of the mixed-mode solutions follows from the analysis of a family of 1D piecewise linear bimodal maps. Finally, the main results of the present paper and the related results in the literature are discussed in Section 4.

2. The model and numerical bifurcation analysis

The Wilson–Callaway model [52] describes the dynamics of the membrane potential and calcium concentration in a multicompartment model of the active dendrite. The variables for each compartment are $v_i(t)$, the voltage, and $u_i(t)$, calcium concentration, taken to be uniform throughout the compartment. The equations in neighboring compartments are coupled through strong electrical coupling. For a two-compartment model, the nondimensional system has the following form:

$$\epsilon\frac{\mathrm{d}v_i}{\mathrm{d}t} = g_1(v_i)(E_1 - v_i) + g_2(u_i)(E_2 - v_i) + \bar{g}_3(E_l - v_i) + d(v_{i+1} - 2v_i + v_{i-1}), \tag{2.1}$$

$$\frac{\mathrm{d}u_i}{\mathrm{d}t} = \omega_i\left(g_1(v_i)(E_1 - v_i) - \frac{u_i}{\tau}\right), \quad i = 1, 2, \quad v_0 = v_1, \quad v_3 = v_2. \tag{2.2}$$

The first three terms in (2.1) represent the intrinsic currents of the compartment. The last term models the electrical coupling between neighboring compartments. Constant $d \gg 1$ is the strength of coupling. The nonlinear conductances are given by the sigmoid functions

$$g_1(v) = \frac{\bar{g}_1}{2}\left(1 + \tanh\left(\frac{v - c_1}{c_2}\right)\right), \tag{2.3}$$

$$g_2(u) = \frac{\bar{g}_2 u^4}{u^4 + c_3}. \tag{2.4}$$

The values of the parameters of (2.1)–(2.4) that we used in our simulations are given in Appendix A. In the Wilson–Callaway model of the dopamine neuron [39,52] the voltage equations are coupled through anisotropic diffusive coupling. Since the mechanism for generating multimodal periodic solutions is independent on the details of the coupling, for simplicity, we consider symmetric coupling in (2.1).

The equations in individual compartments ($d = 0$) result in the phase plane similar to that for the Morris–Lecar system of equations [43] (Fig. 1a). The phase plane analysis shows that for small $\epsilon > 0$ there exists a relaxation limit cycle in the phase plane of each oscillator. The natural frequencies of individual oscillators are proportional to ω_i's and are different in different compartments. The variation in ω_i's is due to the tapering of the dendrite (see [39,52] for details). When the coupling is sufficiently strong the coupled system has an attracting limit cycle with the voltage variables in two compartments being very close (Fig. 1b). When the individual oscillators are close to an AHB. Small changes of the rate of calcium efflux (τ^{-1}) or injected current result in a variety of stable multimodal solutions of the coupled system (Fig. 2). Note that the frequency changes greatly across the family of multimodal solutions (Fig. 3a). We summarize the information about the structure of the family of mixed-mode solutions of (2.1) and (2.2) in Fig. 3b. To classify the multimodal solutions of (2.1) and (2.2), we label them with the symbolic expressions $l_1^{s_1}l_2^{s_2}, \ldots, l_k^{s_k}$, where l_i denotes the number of the large-amplitude oscillations followed by the s_i small-amplitude oscillations. For a given periodic solution with n large and m small-amplitude oscillations within one period, we associate the ratio $n/(n + m)$. We will refer to this ratio as *a firing number*. The firing number is plotted versus

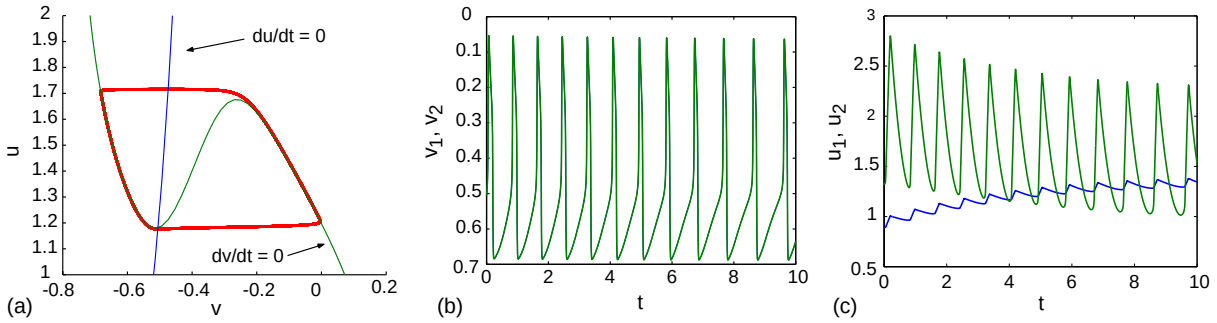

Fig. 1. (a) Phase plane for a single relaxation oscillator (2.1) and (2.2) ($d = 0$): two dashed curves represent nullclines for the voltage and calcium equations, i.e. the sets of points where $\mathrm{d}v_i/\mathrm{d}t = 0$ (S-shaped curve) and $\mathrm{d}u_i/\mathrm{d}t = 0$, respectively. The solid line depicts a limit cycle. Time series plots of $v_{1,2}(t)$ (b) and $u_{1,2}(t)$ (c) for the system of two coupled oscillators (2.1) and (2.2) ($d \gg 1$). Note that the time series in (b) are nearly identical for both oscillators.

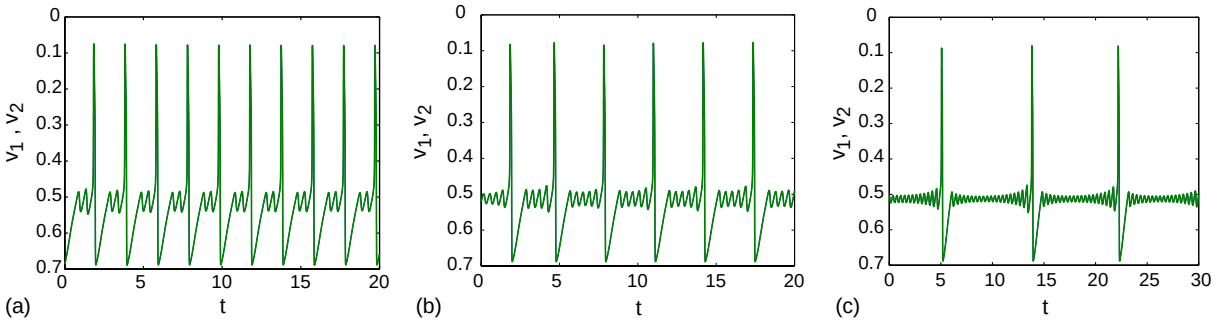

Fig. 2. The mixed-mode periodic solutions of (2.1) and (2.2) for different values of τ (10.3, 10.5, 10.75). The time series of v_1 and v_2 are almost identical.

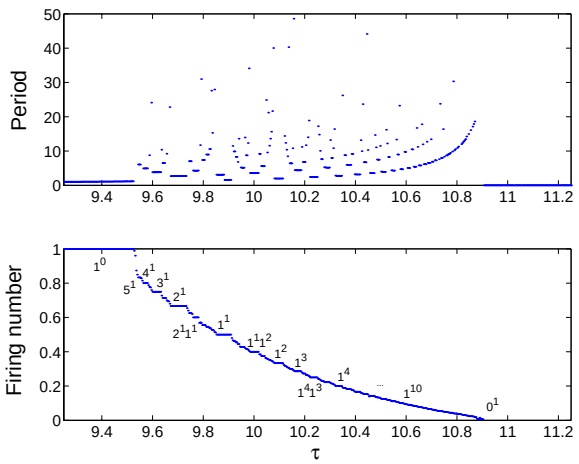

Fig. 3. The top plot shows the variability of the period of the stable periodic solutions of (2.1) and (2.2) under the variation of τ. The firing number plot shows the regions of existence of stable periodic solutions of different topological types.

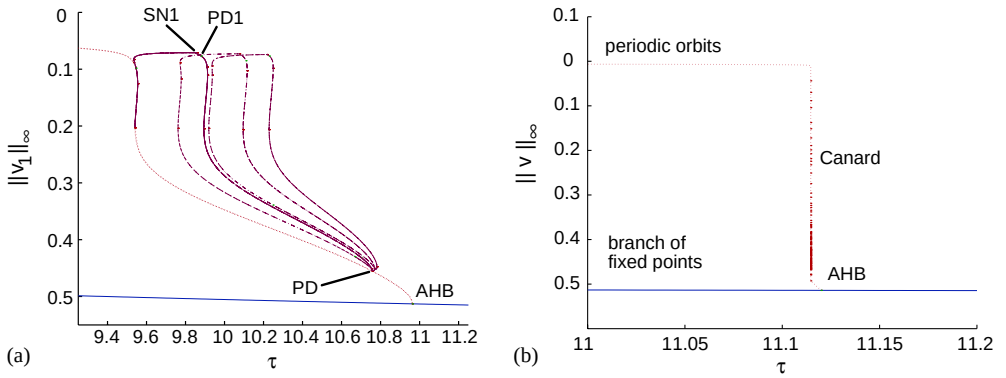

Fig. 4. (a) The bifurcation diagram for the coupled system (2.1) and (2.2): mixed-mode periodic solutions lie on the isolas in the parameter space. AHB, PD, and SN denote Andronov–Hopf, period-doubling, and saddle-node bifurcations, respectively. (b) The bifurcation diagram for a single relaxation oscillator (2.1) and (2.2) ($d = 0$).

a control parameter, τ, in Fig. 3b. This plot shows the sequences of the stable mixed-mode solutions of (2.1) and (2.2). For example, the family of solutions of the form l^1, $l = 1, 2, \ldots, 5$, undergoes a reverse period-adding, as τ is increased, whereas the family of solutions 1^s, $s = 1, 2, \ldots$, exhibits a period-adding phenomenon. By period-adding we mean the increase of the number of oscillations (both large and small amplitude) in one period.

We begin our study of the multimodal regimes in (2.1) and (2.2), with the numerical analysis of the bifurcation structure of the problem. We choose τ as a bifurcation parameter. It is interesting to compare the bifurcation structure of the coupled system (Fig. 4a) with that of a single relaxation oscillator (Fig. 4b). For $\tau > \tau_{\mathrm{AHB}} = 10.96271$, the coupled system has a branch of stable fixed points. At $\tau = \tau_{\mathrm{AHB}}$ the system undergoes a supercritical AHB: the branch of the fixed points becomes unstable and there is a branch of periodic solutions emanating from the AHB (Fig. 4a). Note that for a single relaxation oscillator, small-amplitude relaxation oscillations occupy an $O(\epsilon)$ interval in τ bounded by the AHB point and the rapid transition to the full-amplitude oscillations (canard transition) (Fig. 4b). The corresponding branch emanating from the AHB for the coupled system has a long parabolic segment before the sharp transition to the full-amplitude oscillations. However, the most part of this branch of solutions is unstable. It becomes unstable after a period-doubling bifurcation (PD, Fig. 4a). A blow-up of the region near PD of a more detailed bifurcation diagram is given in Fig. 5b. The upper branch bifurcating from PD carries bimodal periodic solutions. The continuous transformation of solutions lying on this branch is illustrated in Fig. 6. In Fig. 6a we plotted a small-amplitude periodic orbit right before the period-doubling bifurcation PD. Fig. 6b shows a bimodal periodic orbit born at PD. As we track this branch further, the amplitude of one of the component of this solution remains small, while that of the other grows and undergoes a canard transition (Fig. 6b and c). Once the canard transition is complete, the first mixed-mode periodic orbit 1^1 is formed (Fig. 6d). The region of stability of the mixed-mode solution 1^1 lies between a period-doubling bifurcation and a saddle-node bifurcation (PD1 and SN1 in Fig. 4a). The branch of solutions, born at the first period-doubling (PD) bifurcation, eventually closes onto the branch emanating from the AHB (Fig. 4a). By continuation of some other stable multimodal solutions of the form 1^n, we have found that they lie on the closed curves in the parameter space (Fig. 5a). The blow-up in Fig. 5b shows that the only branch connected to the branch emanating from the AHB corresponds to solution 1^1. The regions of stability on the isolas are bounded by the period-doubling and saddle-node bifurcations. In Fig. 5c we plot the isolas corresponding to some other multimodal solutions: 4^1, 3^1, 2^1, etc. Plots in Figs. 3 and 5 suggest several characteristic features of the bifurcation sequences of solutions of (2.1) and (2.2). In the left-hand half of Fig. 3b,

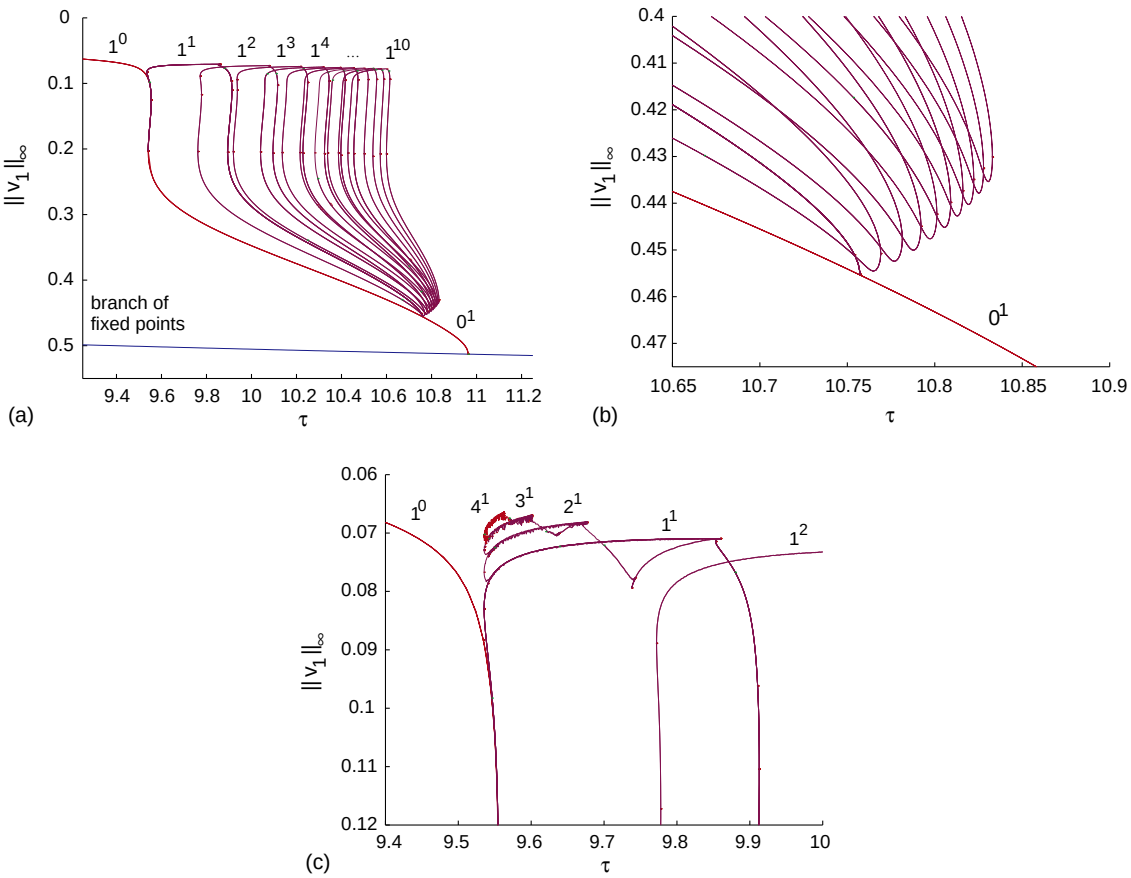

Fig. 5. (a) A more complete bifurcation diagram for the coupled system (2.1) and (2.2). (b) and (c) The blow-ups of two regions of the bifurcation diagram in (a): one near the period-doubling bifurcation (b) and another near the regular relaxation limit cycle 1^0 (c).

there is a sequence of solutions n^1, $n = 5, 4, \ldots, 1$, where n decreases as τ increases. In the middle and right-hand parts of Fig. 3b, we find the sequence of the from 1^m, $m = 1, 2, \ldots$. In Section 4, we will show that these and other properties of the bifurcation sequence of solutions (2.1) and (2.2) follow from the analysis of a family of 1D bimodal maps.

3. Analysis of the system of two coupled oscillators

3.1. The effective equations in the strong coupling limit

The presence of the small parameter $\epsilon > 0$ makes (2.1) and (2.2) a relaxation system. The dynamics of such system can be split into alternating modes: slow motions and fast jumps [24,41]. The slow dynamics is taking place on the (slow) manifold, whose equations to leading order in ϵ are obtained from (2.1) by setting $\epsilon = 0$. To obtain explicit albeit approximate equations for the slow manifold, we linearize $g_2(u)$ about $u = 2$: $g_{2,l}(u) = -au + b$. Function $g_{2,l}(u)$ gives a good approximation to $g_2(u)$ in the range of $u_{1,2}$ near the limit cycle of the coupled system.

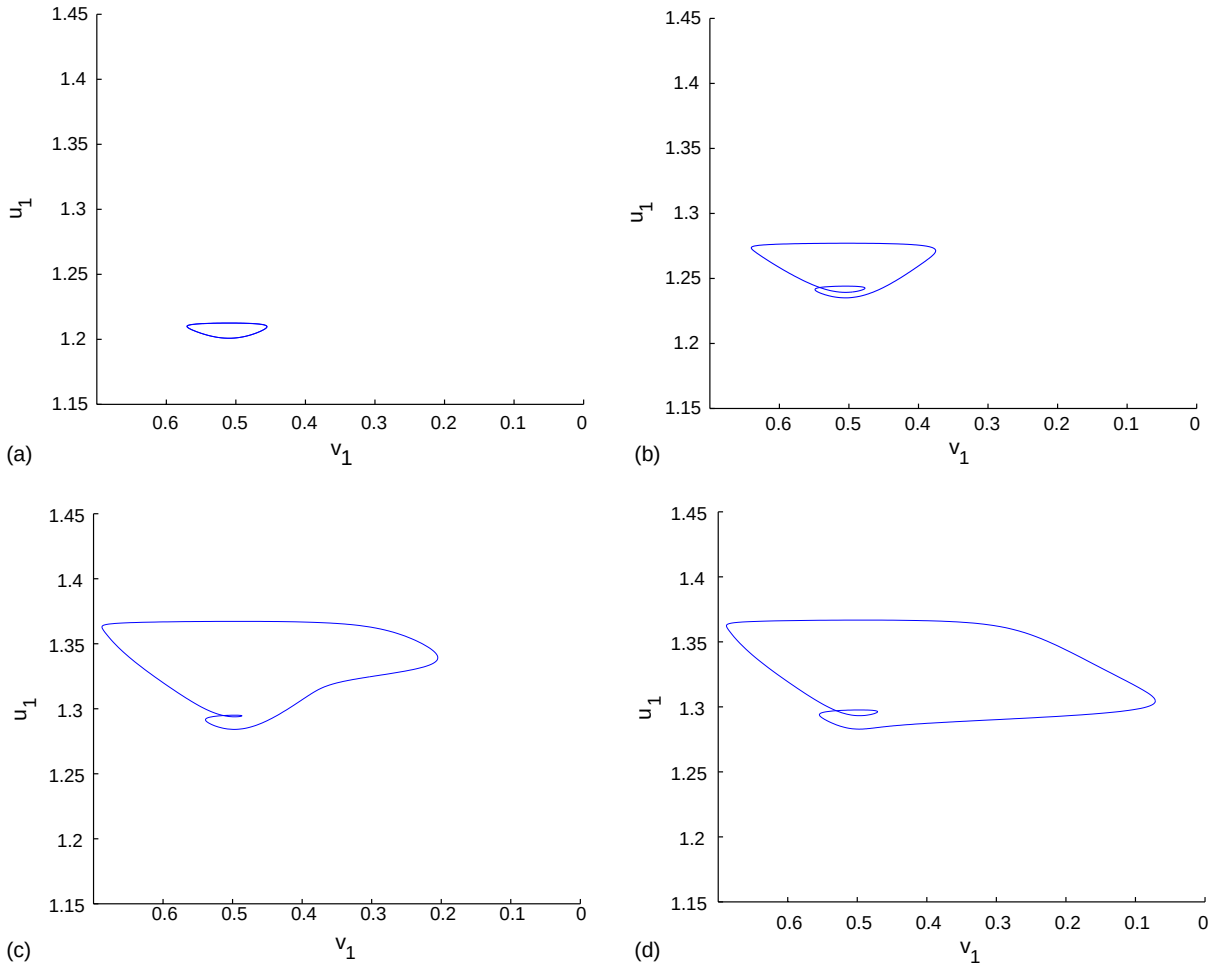

Fig. 6. A series of periodic orbits sampled from the upper branch bifurcating from PD (see Fig. 4a). An unstable bimodal small-amplitude periodic solution in (a) transforms into a stable mixed-mode solution 1^1 in (d) via the canard transition ((b) and (c)).

Using this approximation, we obtain the approximate equations for the slow manifold:

$$u_1 = f(v) + \frac{d(v_2 - v_1)}{a(E_2 - v_1)}, \tag{3.1}$$

$$u_2 = f(v) - \frac{d(v_2 - v_1)}{a(E_2 - v_2)}, \tag{3.2}$$

where

$$f(v) = \frac{g_1(v)(E_1 - v) + \bar{g}_3(E_3 - v)}{a(E_2 - v)} + \frac{b}{a}.$$

In the range of parameters of interest, the graph of $f(v)$ has a qualitatively cubic form. Eqs. (3.1) and (3.2) define a 2D slow manifold, S, in a 4D phase space. The flow on S is described by Eq. (2.2):

$$\frac{\mathrm{d}u_i}{\mathrm{d}t} = \omega_i \left(g_1(v_i)(E_1 - v_i) - \frac{u_i}{\tau} \right), \quad i = 1, 2. \tag{3.3}$$

Off the slow manifold the system dynamics is governed by the fast equations [24,41]. To leading order, the fast equations are obtained by changing time to $s = t/\epsilon$ and setting $\epsilon = 0$:

$$\frac{\mathrm{d}v_i}{\mathrm{d}s} = g_1(v)(E_1 - v_i) + g_2(v_i)(E_2 - v_i) + \bar{g}_3(E_3 - v_i) + d(v_{i+1} - 2v_i + v_{i-1}), \tag{3.4}$$

$$\frac{\mathrm{d}u_i}{\mathrm{d}s} = 0, \quad i = 1, 2, \quad v_0 = v_1, \quad v_3 = v_2. \tag{3.5}$$

As was shown in [39], when the coupling is strong, the dynamics of the coupled system can be reduced to the effective equations for two uncoupled oscillators. This reduction was developed and rigorously justified in [38] for a system of coupled FitzHugh–Nagumo oscillators. For completeness of presentation, we derive the effective equations below.

The asymptotic analysis that follows is based on the following observation. Assuming that the phase trajectory is uniformly bounded for $t \in \mathbb{R}^+$, one can show that for sufficiently large $d > 0$, there exists $t_0 > 0$ (which depends on initial data at $t = 0$) such that

$$|v_2(t) - v_1(t)| \leq C_1\delta, \quad t \geq t_0, \quad \delta = \frac{1}{d}, \tag{3.6}$$

where a positive constant C_1 does not depend on δ (see, e.g., Theorem 7.1 in [38]).

The phase trajectory $(v_1(t), v_2(t), u_1(t), u_2(t))$ undergoes relaxation oscillations. We assume that on each connected component of the slow manifold $v_1(t)$ changes monotonically. This assumption will be easily verified once the asymptotic solution is constructed. Therefore, v_1 can be used to parameterize the trajectory on the slow manifold. Specifically, for any moment of time $\tilde{t}$, by $\mathcal{T} \ni \tilde{t}$ we denote the maximal open interval of time that the trajectory stays on the same connected component of the slow manifold. On $\mathcal{T}$ we define a map $v : t \mapsto v_1(t)$. The coordinates of the phase trajectory for $t \in \mathcal{T}$ can be viewed as functions of v_1:

$$v_i = v_i(v^{-1}(v_1)) \quad \text{and} \quad u_i = u_i(v^{-1}(v_1)), \quad v_1 \in V = v(\mathcal{T}).$$

In particular, we consider the coupling current between the two compartments as a function of v_1:

$$c(v_1) = \frac{d(v_2 - v_1)}{a(E_2 - v_1)}. \tag{3.7}$$

Eqs. (3.6) and (3.7) imply that

$$c(v_1) = \mathrm{O}(1) \quad \text{as } d \to \infty, \tag{3.8}$$

and that on the slow manifold

$$v_2 = v_1 + \delta\chi(v_1), \quad \text{where } \chi(v) = a(E_2 - v)c(v). \tag{3.9}$$

By plugging (3.7) and (3.9) into (3.1), (3.2) and (2.2), we obtain

$$u_1 = f(v_1) + c(v_1), \qquad u_2 = f(v_1 + \delta\chi(v_1)) - c(v_1),$$
$$\frac{\mathrm{d}u_1}{\mathrm{d}t} = \omega_1\left(g(v_1) - \frac{1}{\tau}u_1\right), \qquad \frac{\mathrm{d}u_2}{\mathrm{d}t} = \omega_2\left(g(v_1 + \delta\chi(v_1)) - \frac{1}{\tau}u_1\right). \tag{3.10}$$

Eqs. (3.10) describe the slow dynamics of (2.1) and (2.2) for any interval of time that the phase trajectory spends on the slow manifold.

To use (3.10) we need to find $c(v_1)$. By differentiating both sides of the first two equations in (3.10) with respect to v_1 and rewriting the last two equations, we have

$$u_1' = f'(v_1) + c'(v_1), \qquad u_2' = f'(v_1 + \delta\chi(v_1))(1 + \delta\chi'(v_1)) - c'(v_1),$$
$$u_1' = \omega_1 \left(g(v_1) - \frac{1}{\tau} u_1 \right) \left(\frac{\mathrm{d}v_1}{\mathrm{d}t} \right)^{-1}, \qquad u_2' = \omega_2 \left(g(v_1 + \delta\chi(v_1)) - \frac{1}{\tau} u_1 \right) \left(\frac{\mathrm{d}v_1}{\mathrm{d}t} \right)^{-1},$$

where $\phi' = \mathrm{d}\phi/\mathrm{d}v_1$. By setting equal the ratios of the first and last pairs of equations above, we arrive at a nonlinear differential equation for $c(v_1)$:

$$\frac{f'(v_1) + c'(v_1)}{f'(v_1 + \delta\chi(v_1))(1 + \delta\chi'(v_1)) - c'(v_1)} = \frac{\omega_1 (g(v_1) - \tau^{-1} u_1)}{\omega_2 (g(v_1 + \delta\chi(v_1)) - \tau^{-1} u_2)}. \tag{3.11}$$

The approximate solution of (3.11) is found by disregarding $\mathrm{O}(\tau^{-1}, \delta)$ terms

$$c(v_1) = c_0(v_1) + \mathrm{O}\left(\delta, \frac{1}{\tau} \right) = \frac{\omega_1 - \omega_2}{\omega_1 + \omega_2} f(v_1) + K + \mathrm{O}\left(\delta, \frac{1}{\tau} \right), \tag{3.12}$$

where a constant of integration K will be specified later. By construction of $c(v_1)$, K is defined only for the time the phase trajectory stays on the same component of the slow manifold.

By plugging (3.12) into (3.10), to leading order we obtain

$$u_i = \xi_i f(v_1) + \sigma_i K, \qquad \frac{\mathrm{d}u_i}{\mathrm{d}t} = \omega_i \left(g(v_1) - \frac{1}{\tau} u_i \right), \tag{3.13}$$

where

$$\sigma_i = (-1)^{i+1}, \qquad \xi_i = \frac{\omega_i}{\bar{\omega}}, \quad \bar{\omega} = \frac{\omega_1 + \omega_2}{2}, \quad i = 1, 2.$$

With the appropriate choice of K, Eqs. (3.13) describe the projections of the slow dynamics onto the u_i–v_i phase planes. The projections of the fast vector field onto u_i–v_i planes are easily obtained from (3.4) and (3.5). Thus, we can describe the dynamics of the fast–slow system (3.1)–(3.5) in terms of its projections to the u_i–v_i planes. The dynamics in the phase planes of individual oscillators admits a simple geometric description. For this, in the u_i–v_i phase planes, we define the generalized nullclines [38]

$$\Gamma_i(K) = \{(u_i, v_i) : u_i = \xi_i f(v_i) + \sigma_i K\}$$

(see Fig. 7). Recall that $v_1 = v_2$ as $\delta \to 0$. Therefore, the projections of the phase point to u_i–v_i, move along $\Gamma_i(K)$, $i = 1, 2$, and jump simultaneously, whenever in one of the phase planes the jump point is reached. To determine K we use the first pair of equations in (3.13):

$$K = \frac{\omega_2 \tilde{u}_1 - \omega_1 \tilde{u}_2}{\omega_1 + \omega_2},$$

where $\tilde{u}_{1,2}$ denote the values of the slow variables prior to landing to a given component of the slow manifold. To determine K, $u_{1,2}$ in (3.13) can be chosen at other moments of time. The different choices yield within $\mathrm{O}(\tau^{-1})$ accuracy the same value of K. Suppose, for a given K, the effective phase planes for the first and the second oscillator contain relaxation limit cycles $Z_1(K)$ and $Z_2(K)$, respectively (see Fig. 7). Then on the time interval of $\mathrm{O}(1)$, the phase trajectory of the coupled system will undergo relaxation oscillations in the $\mathrm{O}(\tau^{-1})$ neighborhood of $Z(K) = Z_1(K) \times Z_2(K)$. For longer times, the value of K needs to be adjusted for Eqs. (3.13) and (3.3) to remain a good approximation for the dynamics of the coupled system. The procedure for updating K will be given

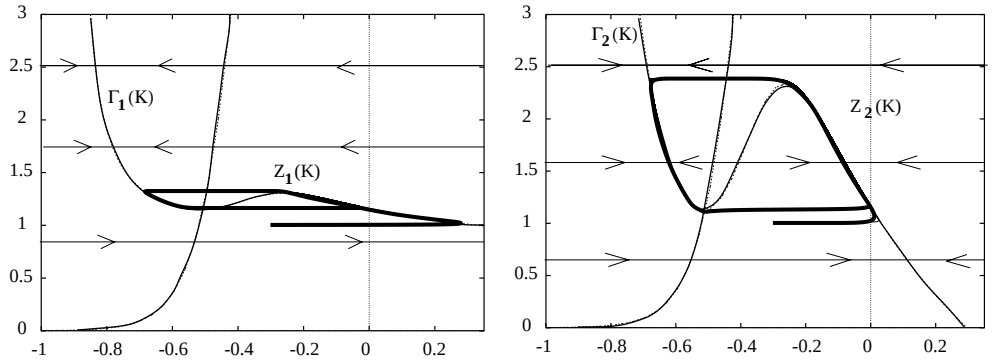

Fig. 7. Effective phase planes for individual oscillators.

later. Therefore, for large d, τ, the phase trajectory of the coupled system stays close to a cylinder foliated by a one-parameter family of periodic orbits $Z(K)$ of the approximate system. This family plays a central role in the description of the dynamics of (2.1) and (2.2).

We shall refer to the phase portraits generated by the slow equations (3.13) and the fast vector field as the *effective phase planes*. The dynamical equations defining such fast–slow dynamics in the phase planes of individual oscillators will be called *the effective equations* for the first and the second oscillators:

$$\epsilon \frac{\mathrm{d}v_i}{\mathrm{d}t} = a(E_2 - v_i)(\xi_i f(v_i) - u_i + \sigma_i K), \tag{3.14}$$

$$\frac{\mathrm{d}u_i}{\mathrm{d}t} = \omega_i \left(g(v_i) - \frac{1}{\tau} u_i \right), \quad i = 1, 2, \tag{3.15}$$

where

$$g(v) = g_1(v)(E_1 - v). \tag{3.16}$$

3.2. System dynamics near an AHB

We are interested in the dynamics of the coupled system when individual oscillators are close to an AHB. To this end, we review some facts about the AHB for a 2D relaxation oscillator (3.14) and (3.15). In particular, for each oscillator we specify two values of K: the AHB point, K^{H}, and the canard point, K^{c}. The former corresponds to the value of K, at which the AHB takes place for the effective equations of an individual oscillator, and the latter corresponds to the sharp transition in the amplitude of the limit cycle born at the AHB. Both values can be effectively estimated using the geometric theory for relaxation oscillations [31] or asymptotic expansions [2,3]. In the present section and in Appendix B, we omit the indices referring to individual oscillators, since the effective equations for both oscillators (3.14) and (3.15) are of the same form.

The results of Krupa and Szmolyan [31] imply that as K is varied the effective oscillators (3.14) and (3.15) undergo an AHB and a canard transition at

$$K^{\mathrm{H}} = K^0 + \tfrac{1}{2}\sigma\beta\epsilon + \mathrm{O}(\epsilon^{3/2}), \tag{3.17}$$

$$K_i^{\mathrm{c}} = K^0 + \sigma \left\{ \frac{\beta}{4} - \frac{\beta^2 \tau E}{\omega} \left[\frac{f_3}{f_2} - \frac{g_2}{g_1} \right] \right\} \epsilon + \mathrm{O}(\epsilon^{3/2}), \tag{3.18}$$

respectively, where $\bar{v}$ is the point of local minimum of $f(v)$ and $K^0 = \tau g(\bar{v}) - \xi f(\bar{v})$. Constants α, β, and E are defined in Appendix B. Here and below by f_i and g_i, $i = 1, 2, \ldots$, we denote the values of the ith derivatives of $f(v)$ and $g(v)$ at $v = \bar{v}$. Moreover, if

$$\frac{\xi f_2}{\tau g_1} + \frac{f_3}{f_2} - \frac{g_2}{g_3} < 0, \quad i = 1, 2, \tag{3.19}$$

the AHB is supercritical (see Appendix B for details). Henceforth, we assume that (3.19) is satisfied.

We will also refer to another two values of K for each oscillator, K^{r} and K^{s}, which separate the canard solutions from the full-amplitude relaxation oscillations and from small-amplitude oscillations near the AHB, respectively. For $\epsilon > 0$ sufficiently small and for fixed $\nu \in (0, 1)$, such values are defined in Theorem 3.3 of [31]. Moreover, for $K^{\mathrm{r,s}}$, we have (see [31]):

(a) $|K^{\mathrm{r}} - K^{\mathrm{s}}| \leq \exp\{-1/\epsilon^{1-\nu}\}$,
(b) the v-amplitudes of the small oscillations that are not canards are $\mathrm{O}(\epsilon^{1-\nu})$.

3.3. The Lyapunov function

As we have shown in Section 3.2, the dynamics of the coupled system can be characterized as synchronous relaxation oscillations around the cycles $Z(K) = Z_1(K) \times Z_2(K)$ superimposed on the slow drift in K. The goal of the present and the following sections is to estimate the rate of this drift. For this we assume that the phase trajectory of the coupled system is in the neighborhood of $Z(K)$ and introduce the following function:

$$L(u_1, u_2) = \frac{1}{2}\left(\frac{u_1}{\omega_1} - \frac{u_2}{\omega_2} + A\right)^2, \tag{3.20}$$

where

$$A = \frac{1}{T}\frac{\omega_1 - \omega_2}{\omega_1\omega_2}\int_0^T f(v_1(t))\,\mathrm{d}t,$$

T is a period of oscillations around $Z(K)$, and $f(v_1)$ is evaluated on the periodic orbit $Z(K)$. Note that $Z(K)$ and T depend on K, where K is changing adiabatically.

Next, we evaluate the change of L, ΔL, after the trajectory goes around the limit cycle $Z(K)$ once. For this, we compute

$$\frac{\mathrm{d}L}{\mathrm{d}t} = \left(\frac{u_1}{\omega_1} - \frac{u_2}{\omega_2} + A\right)\left(\frac{\dot{u}_1}{\omega_1} - \frac{\dot{u}_2}{\omega_2}\right) = \left(\frac{u_1}{\omega_1} - \frac{u_2}{\omega_2} + A\right)\left([g(v_1) - g(v_2)] - \frac{1}{\tau}[u_1 - u_2]\right). \tag{3.21}$$

On the slow segments of $Z(K)$, by (3.10) and (3.13), to leading order we have

$$\frac{u_1}{\omega_1} - \frac{u_2}{\omega_2} = \frac{\xi_1 f(v_1) + K}{\omega_1} - \frac{\xi_2 f(v_1) - K}{\omega_2} = \frac{\omega_1 + \omega_2}{\omega_1\omega_2}K, \qquad u_2 - u_1 = -2c(v_1),$$

and, by the mean value theorem and (3.7),

$$g(v_1) - g(v_2) = g'(\eta)(v_1 - v_2) = -\delta g'(\eta)a(E_2 - v_1)c(v_1) \quad \text{for some } (\eta, \zeta) \in Z_1(K).$$

By plugging in these formulas into (3.21) and by noting that $\delta \ll \tau^{-1}$ (see Appendix A), we obtain

$$\frac{\mathrm{d}L}{\mathrm{d}t} = -\frac{2}{\tau}c(v_1)\left(\frac{\omega_1 + \omega_2}{\omega_1\omega_2}K + A\right) + \text{higher order terms (h.o.t.)}. \tag{3.22}$$

Eqs. (3.21) and (3.22) yield

$$\frac{\mathrm{d}L}{\mathrm{d}t} = -\frac{2}{\tau}\left(\frac{\omega_1+\omega_2}{\omega_1\omega_2}K + A\right)\left(\frac{\omega_1-\omega_2}{\omega_1+\omega_2}f(v_1) + K\right) + \text{h.o.t. for some } (\zeta,\eta)\in Z. \tag{3.23}$$

By integrating (3.23) over one period of oscillations, to leading order, we have

$$\Delta L = \frac{-2T}{\tau}\left(\frac{\omega_1+\omega_2}{\omega_1\omega_2}K + A\right)\left(\frac{\omega_1-\omega_2}{\omega_1+\omega_2}\frac{1}{T}\oint_Z f(v_1)\,\mathrm{d}s + K\right) = \frac{-1}{\tau}\frac{\omega_1\omega_2}{\bar{\omega}}T\left(\frac{\omega_1+\omega_2}{\omega_1\omega_2}K + A\right)^2. \tag{3.24}$$

Finally, we use (3.13) to express L as a function of K:

$$L(K) = \frac{1}{2}\left(\frac{\omega_1+\omega_2}{\omega_1\omega_2}K + A\right)^2 + \text{h.o.t.} \tag{3.25}$$

The combination of (3.24) and (3.25) yields

$$\Delta L = \frac{-2}{\tau}\frac{\omega_1\omega_2}{\bar{\omega}}TL(K) + \text{h.o.t.} \tag{3.26}$$

Eq. (3.26) implies that in the strong coupling limit the rate of approach of the trajectory of the coupled system to the limit cycle is proportional to τ^{-1}.

3.4. The Poincare map

From (3.26) we extract a map $\tilde{K} = P(K)$ for the change of K after one cycle of oscillations. By differentiating (3.25), to leading order we have

$$L'(K) = \frac{\omega_1+\omega_2}{\omega_1\omega_2}\left[\frac{\omega_1+\omega_2}{\omega_1\omega_2}K + A\right].$$

The expression above and (3.26) yield an estimate for the correction in K after one cycle of oscillations:

$$\Delta K = \frac{\Delta L}{L'(K)} = \frac{-2T}{\tau}\left(\frac{\omega_1\omega_2}{\omega_1+\omega_2}\right)^2\left(\frac{\omega_1+\omega_2}{\omega_1\omega_2}K + A\right).$$

Therefore,

$$\tilde{K} = P(K) = \left(1 - \frac{2\omega_1\omega_2}{\omega_1+\omega_2}\frac{T}{\tau}\right)K + \frac{2\omega_1\omega_2(\omega_2-\omega_1)}{\tau(\omega_1+\omega_2)^2}\int_0^T f(v_1(t))\,\mathrm{d}t.$$

We rewrite the expression above as

$$\tilde{K} = P(K) = \left(1 - \frac{1}{\tau}\Omega_1 T\right)K + \frac{1}{\tau}\Omega_2 T\bar{f}, \tag{3.27}$$

where

$$\Omega_1 = \frac{\omega_1\omega_2}{\bar{\omega}}, \qquad \Omega_2 = \Omega_1\frac{\omega_2-\omega_1}{2\bar{\omega}} \quad \text{and} \quad \bar{f} = \frac{1}{T}\int_0^T f(v_1(t))\,\mathrm{d}t.$$

To interpret (3.27) we review the geometric interpretation of the reduced system (3.13). The phase points in the effective phase planes u_i–v_i move along the stable portions of $\Gamma_i(K)$, $i = 1, 2$ (see Fig. 7). According to (3.9), there is an $\mathrm{O}(\delta)$ lag between the effective oscillators. When in one of the phase planes the jump point is reached, this indicates that the phase point of the coupled system hit the boundary of the stable portion of the slow manifold and

the fast jump follows. Therefore, the fast jumps take place in *both* effective phase planes, when the jump point is reached in *one* of them. If $Z_i(K)$, $i = 1, 2$, are full-amplitude relaxation limit cycles as shown in Fig. 7, their shapes to leading order do not depend on the fact what oscillator initiates the jump. In this case, we use either effective phase plane to determine the period of oscillations, T, and the average value of f, $\bar{f}$, and obtain the change of K after one cycle of oscillations from (3.27). A similar situation was analyzed in [38], where a map for K was derived using a different method. The situation is different when one of $Z_i(K)$, $i = 1, 2$, is a canard cycle. In this case, the position of the jump point is critical for the shape of the corresponding limit cycle $Z_i(K)$. Therefore, it is important to know what oscillator triggers the jump, because it determines the behavior of the coupled system. In this case, we use the phase plane of such oscillator to determine the values of T and $\bar{f}$ in (3.27). We denote the map obtained from (3.27) using the effective phase plane of oscillator i by $P_i(K)$. For a given cycle of oscillations, we call the oscillator, in whose phase plane the jump point is reached first, a *dominant* oscillator. In general, it is possible that each of the oscillators is dominant for different portions of the period. Then the resultant map for K is given by

$$P(K) = \begin{cases} P_1(K) & \text{if the first oscillator is dominant,} \\ P_2(K) & \text{if the second oscillator is dominant.} \end{cases} \tag{3.28}$$

The value of K determines the position of the phase trajectory on the cylinder foliated by the periodic orbits $Z(K) = Z_1(K) \times Z_2(K)$. Map $P(K)$ provides the change of K after one cycle of oscillations. In this sense, $P(K)$ can be viewed as a Poincare map. In fact, we recall that the dynamics on the slow manifold is constrained by the equations

$$u_1 = \xi_1 f(v_1) + K \quad \text{and} \quad u_2 = \xi_2 f(v_2) - K, \tag{3.29}$$

where $v_1 = v_2$ as $\delta \to 0$. With these constraints, the Poincare map for a 4D degenerate system (3.1)–(3.5) is one-dimensional. Moreover, from (3.29) K is easily expressed in terms of the phase coordinates:

$$K = \frac{\omega_2 u_1 - \omega_1 u_2}{\omega_1 + \omega_2}.$$

Therefore, $P(K)$ is a Poincare map for the degenerate system (3.1)–(3.5) written in a special system of coordinates after the dimension reduction of Section 3.1. The periodic solutions of (2.1) and (2.2) correspond to the fixed points and cycles of (3.27). The latter determine the multimodal periodic orbits. The structure of P and and the form of its dependence on τ explain the bifurcations of the multimodal periodic solutions of (2.1) and (2.2).

As will be evident from the analysis in the following section, (3.28) defines a multimodal map, which can be approximated by a piecewise linear multivalued map. However, in the Wilson–Callaway model with parameters given in Appendix A, for the most part of the domain of existence of the multimodal periodic solutions, the second oscillator is dominant, i.e. $P(K) = P_2(K)$. We postpone the argument showing this until Section 3.6.

3.5. The piecewise linear approximation of the Poincare map

In the present section, we study the case when $P(K)$ coincides with $P_2(K)$. In particular, we study the existence of attracting cycles of $P_2(K)$, and their bifurcations under the variation of τ. Unless stated otherwise, all constants and variables used in this section refer to the effective equations of the second oscillator.

In the neighborhood of K^c, the period of the stable limit cycle $Z_2(K)$ (in the effective phase plane for the second oscillator) and the average value of f, $\bar{f}$, (3.27) change drastically (see Fig. 8a and b). To study $P(K)$ in the neighborhood of K^c, it is convenient to rescale $K = K^c + \epsilon k$:

$$\tilde{k} = \left(1 - \frac{1}{\tau}\Omega_1 T\right) k + \frac{1}{\tau}\Omega_1 T \frac{1}{\epsilon}\left[\frac{\Omega_2}{\Omega_1}\bar{f} - K^c\right]. \tag{3.30}$$

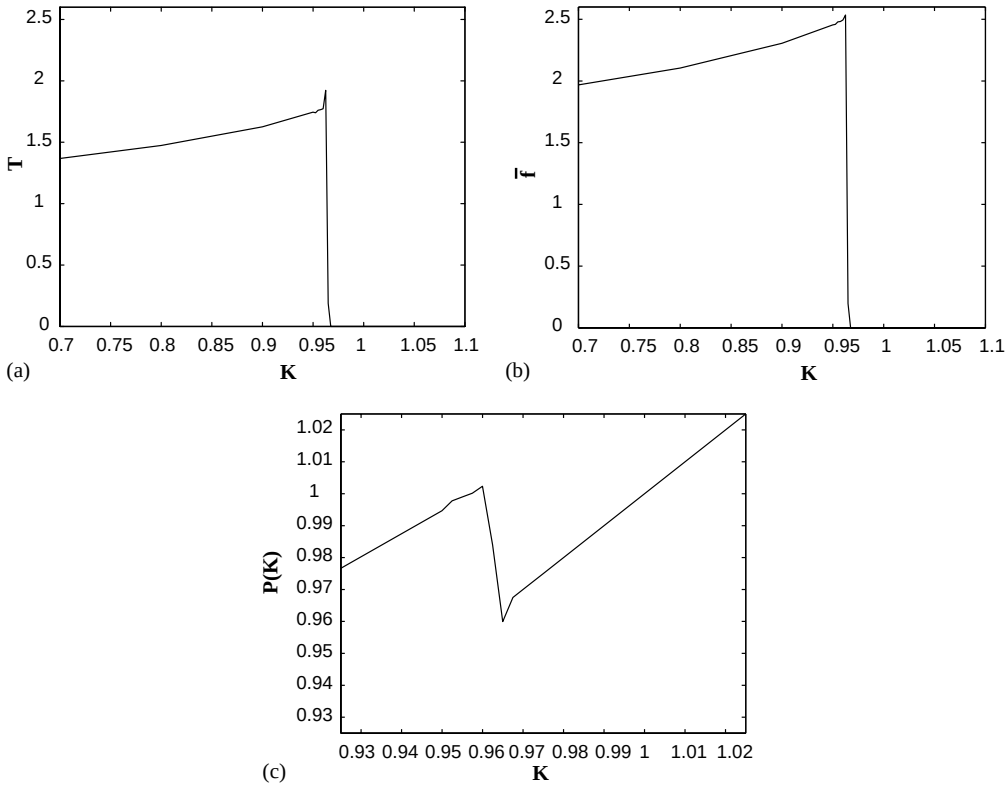

Fig. 8. The period of oscillations, T (a), and the average value of f, $\bar{f}$ (b), are plotted for effective equations for the second oscillator near an AHB. (c) The resultant map (3.27).

We recall the values of $K^{r,s}$ which separate the canard cycles from the full-amplitude relaxation oscillations ($K < K^{r}$) and the small-amplitude oscillations near the AHB ($K^{s} < K < K^{H}$) (see Section 3.2). In the neighborhood of K^{c}, we construct a piecewise linear approximation of (3.27). First, we note that the size of (K^{r}, K^{s}) is exponentially small and we shrink it to a point K^{c} ($k = 0$). For $k < 0$ ($K < K^{c}$), we approximate (3.30) by evaluating T and $\bar{f}$ at K^{r}. Similarly, we approximate (3.30) for $k > 0$ ($K^{c} < K < K^{H}$) by evaluating T and $\bar{f}$ at K^{s}. Thus, we arrive at a piecewise linear approximation of (3.30):

$$\tilde{k} = \begin{cases} (1 - a^{r})k + a^{r}\phi^{r}, & k < 0, \\ (1 - a^{s})k + a^{s}(\phi^{r} - \Phi), & k > 0, \end{cases} \tag{3.31}$$

where

$$a^{r,s} = \frac{1}{\tau}\Omega_1 T^{r,s}, \qquad \phi^{r} = \frac{1}{\epsilon}\left(\frac{\Omega_2}{\Omega_1}\bar{f}^{r,s} - K^{c}\right), \qquad \Phi = \frac{\Omega_2}{\Omega_1}\{\bar{f}^{r} - \bar{f}^{s}\}.$$

Note that $\bar{f}^{r} = O(1)$, $\Phi = O(1)$ and K^{c} depends on τ (see (3.18)).

Suppose, for a given $\tau > 0$, $\Omega_2\Omega_1^{-1}\bar{f}^{r} < K^{c}$. Then (3.31) has a unique attracting fixed point, which corresponds to the limit cycle of the coupled system. When τ is increased K^{c} is decreasing and at some value of τ, $\Omega_2\Omega_1^{-1}\bar{f}^{r}$ and K^{c} coincide. This corresponds to a bifurcation of the stable limit cycle. Below we show that as $\Omega_2\Omega_1^{-1}\bar{f}^{r}$ is passing through the $O(\epsilon)$ neighborhood of K^{c} (i.e., $\phi^{r} \sim O(1)$, $\phi^{r} > 0$), (3.31) has a family of attracting cycles.

Under the variation of τ the value of ϕ^{r} in (3.31) changes. To study the bifurcations of cycles of (3.31) as ϕ^{r} is varied, we change the independent variable to

$$x = \frac{k}{\varsigma}, \quad \varsigma = a^{\mathrm{r}}\phi^{\mathrm{r}} + a^{\mathrm{s}}(\Phi - \phi^{\mathrm{r}}). \tag{3.32}$$

In new variables, the Poincare map takes the following form:

$$\tilde{x} = P_\lambda(x) = \begin{cases} P_{\lambda,l}(x) \equiv lx + \lambda, & x < 0, \\ P_{\lambda,r}(x) \equiv rx + \lambda - 1, & x > 0, \end{cases} \tag{3.33}$$

where $l, r = 1 - a^{\mathrm{r,s}} < 1$ are positive constants and $\lambda = a^{\mathrm{r}}\phi^{\mathrm{r}}/\varsigma$ is the control parameter. P_λ maps the interval $I_\lambda = [\lambda - 1, \lambda]$ into itself. By a simple translation $y = x - 1 + \lambda$, P_λ can be transformed into a map of a unit interval into itself, but it is convenient to work with P_λ in its present form (3.33). The dependence of I_λ on λ may be ignored. Similarly, one can derive a piecewise linear approximation of the Poincare map for the first oscillator, but we are not going to use it in our analysis.

Bimodal maps and their piecewise linear approximations similar to (3.33) arise, for example, in the context of forced relaxation oscillations [33]. They possess a rich bifurcation structure. The bifurcation phenomena in the families of these maps have been studied numerically and analytically [12,25,28,33–35,37,40,44,45,53]. When $l = r$ the bifurcation structure of (3.23) was analyzed in [12]. It was shown in [12] that for almost all values of $\lambda \in [0, 1]$ the map (3.33) (with $l = r$) has attracting periodic orbits. The complimentary set in λ has fractal dimension 0. Leaving the analytical study of (3.33) with $l \neq r$ for the future investigation, we illustrate several properties of the bifurcation sequences in (3.33) by considering simple periodic orbits 1^p (p^1), $p \in \mathbb{N}$. We show that these families of periodic orbits exhibit period-adding and phenomena.

Theorem 3.1. *Let $0 < l, r < 1$. Then (3.33) has an attracting cycle p^1 (1^p), $p \in \mathbb{N}$, iff $\underline{\lambda}(p) < \lambda \leq \bar{\lambda}(p)$ ($\underline{\mu}(p) \leq \lambda < \bar{\mu}(p)$), where*

$$\underline{\lambda}(p) = \frac{l^p(1-l)}{1-l^{p+1}}, \qquad \bar{\lambda}(p) = \frac{l^{p-1}(1-l)}{1-l^p + rl^{p-1}(1-l)}, \tag{3.34}$$

$$\underline{\mu}(p) = 1 - \frac{r^{p-1}(1-r)}{1-r^p + lr^{p-1}(1-r)}, \qquad \bar{\mu}(p) = 1 - \frac{r^p(1-r)}{1-r^{p+1}}. \tag{3.35}$$

Moreover,

$$\underline{\lambda}(p+1) < \bar{\lambda}(p+1) < \underline{\lambda}(p) < \bar{\lambda}(p), \tag{3.36}$$

$$\bar{\mu}(p) < \underline{\mu}(p) < \bar{\mu}(p+1) < \underline{\mu}(p+1). \tag{3.37}$$

Proof. See Appendix C. □

As follows from Theorem 3.1, for small values of $\lambda > 0$, the family of maps (3.33) possesses attracting cycles with large number of points on the left-hand branch and one point on the right-hand branch (Fig. 9a). Relations (3.36) imply that, as λ increases, the family of cycles p^1 undergo reverse period-adding (Fig. 9b). Finally, as λ is increased further, we find periodic orbits of the type 1^p, exhibiting period-adding (Fig. 9c), as follows from (3.37). This information is summarized in Fig. 10, where we plot *the generalized winding number* computed on periodic orbits of (3.33) for different values of λ. For a cycle of (3.33) with m points on the left-hand branch and n points on the right-hand branch, *the generalized winding number* is given by the ratio $n/(n+m)$. The plots in Figs. 3b

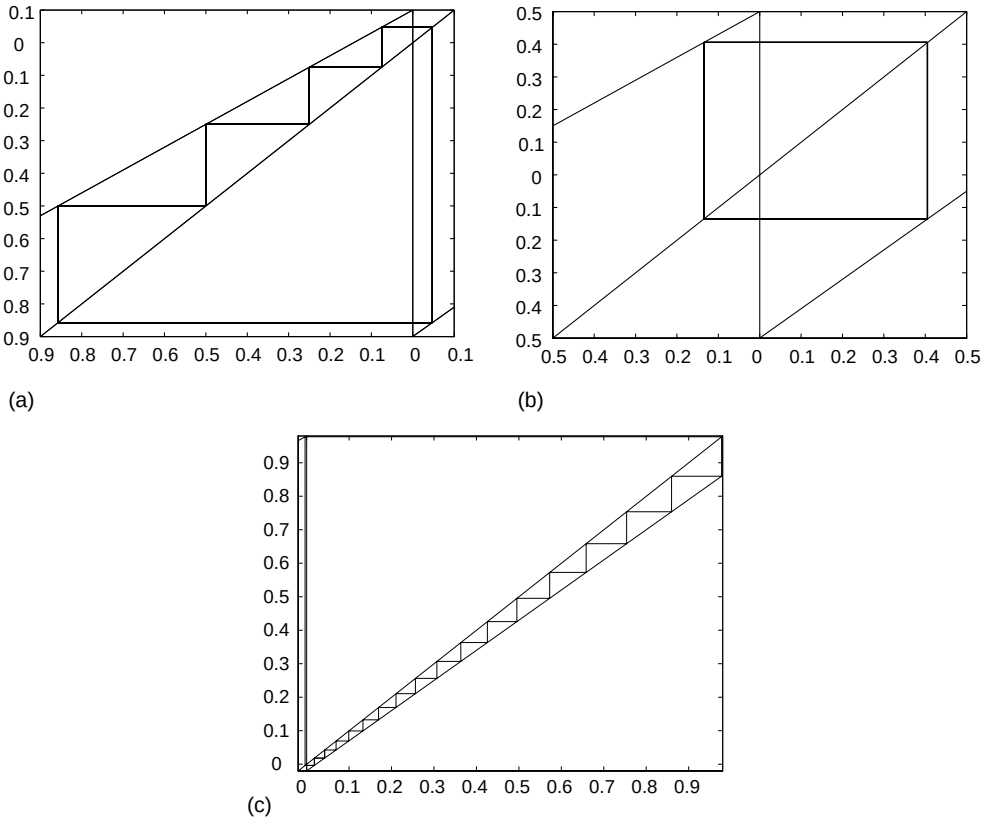

Fig. 9. Cycles of the bimodal piecewise linear map (3.33) for increasing values of $\lambda \in [0, 1]$.

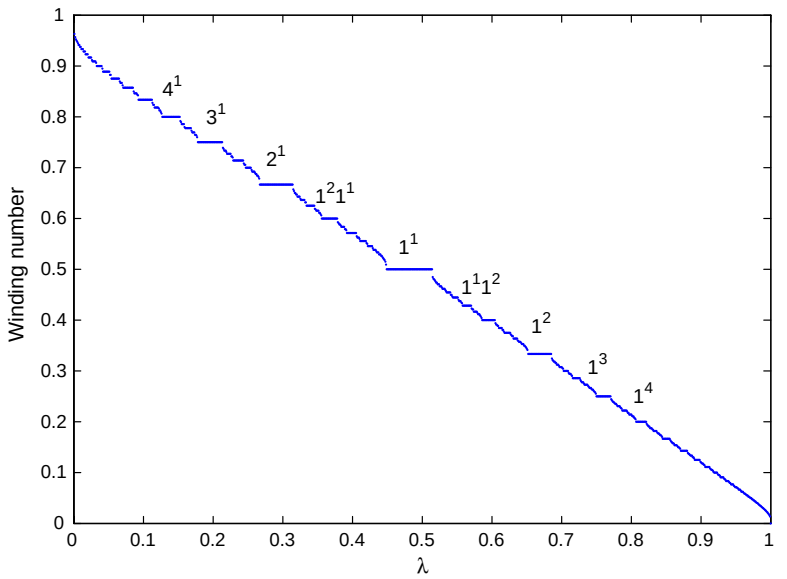

Fig. 10. The generalized winding number for periodic orbits of the family of maps (3.33).

and 10 show similar sequences of topological types of solutions in the continuous and discrete systems, confirming our analytical results. Thus, when $P = P_2$, the family of maps (3.31) explain the order in which different multimodal periodic orbits appear in (2.1) and (2.2) under the variation of τ. In the next section, we justify taking $P = P_2$ and specify the region where this relation holds.

3.6. Determining a dominant oscillator

The problem of determining a dominant oscillator requires carrying out the asymptotic analysis in the effective phase planes near the fixed points to the next order ($O(\tau^{-1})$, as $\tau \to \infty$). However, the limit $\tau \to \infty$ is not physical in the context of the Wilson–Callaway model, because τ^{-1} represents the rate of calcium efflux and it cannot be taken to zero. Besides, changing τ, as required in the limiting process $\tau \to \infty$, not only affects the terms in the asymptotic expansions of solutions, but also changes the positions of the u-nullclines ($u_i = \tau g(v_i)$) in the effective phase planes, and, therefore, changes the positions of the fixed points. The latter are critical for the structure of the multimodal solutions discussed in this paper. For these reasons, we do not pursue a rigorous treatment of this problem and resort to an approximate calculation. The argument below relies on the assumption that the v-coordinates of the jump points in the effective phase planes of two oscillators are close to each other. For small $\epsilon > 0$ and $\tau^{-1} > 0$, this assumption is justified by the nullcline configurations in the effective phase planes and is consistent with our numerics. Then the dominant oscillator is the one that travels ahead of the other on the slow manifold near the fixed point. In the remainder of this section, we show that in the range of parameters used in the Wilson–Callaway model, the second oscillator is dominant for the most part of the interval in τ, in which the multimodal solutions of (2.1) and (2.2) exist. Therefore, the structure and bifurcations of this part of the family of the multimodal solutions are determined by $P_2(K)$.

Recall that by (3.9), there is a small phase difference between the two oscillators:

$$v_2 - v_1 = \delta\chi(v_1), \quad \text{where } \chi(v) = a(E_2 - v)c(v). \tag{3.38}$$

This phase difference plays a little role for the most part of the slow dynamics, but it is important for the dynamics near the jump point, $v \approx \bar{v}$. Because $a(E_2 - \bar{v}) > 0$, (3.38) implies that the sign of the difference $(v_2 - v_1)$ is the same as that of $c(v_1)$. Below we show that, for a large part of the family of stable multimodal solutions of (2.1) and (2.2), $c(v_1) > 0$ near the jump point.

Let us consider a stable multimodal limit cycle of the coupled system

$$Z = Z(\bar{K}) \cup Z(\bar{K}_1) \cup Z(\bar{K}_2) \cup \cdots \cup Z(\bar{K}_s),$$

where $Z(\bar{K}_i)$, $i = 1, 2, \ldots, s$ stand for the small-amplitude oscillations and $Z(\bar{K})$ denotes a large-amplitude part of the limit cycle. For simplicity, we assume that Z contains one large-amplitude oscillation. By Z_j, $Z_j(\bar{K})$, and $Z_j(\bar{K}_i)$, $j = 1, 2$, $i = 1, 2, \ldots, s$, we denote the projections of Z, $Z(\bar{K})$, and $Z(\bar{K}_i)$ onto the phase plane of the jth oscillator. Since Z is a limit cycle of the coupled system, the change of L after one period of oscillations, ΔL, to leading order is 0. Then Eq. (3.22) implies that, on Z, to leading order we have

$$\int_0^T c(v_1(t))\,\mathrm{d}t = 0, \tag{3.39}$$

i.e. the average value of $c(v_1)$ is zero. By differentiating (3.13) with respect to t and using (2.2), on the slow manifold, we relate

$$\mathrm{d}t = \frac{f'(v_1)\,\mathrm{d}v_1}{\bar{\omega}(g(v_1) - \tau^{-1}(\xi_1 f(v_1) + \bar{K}))}. \tag{3.40}$$

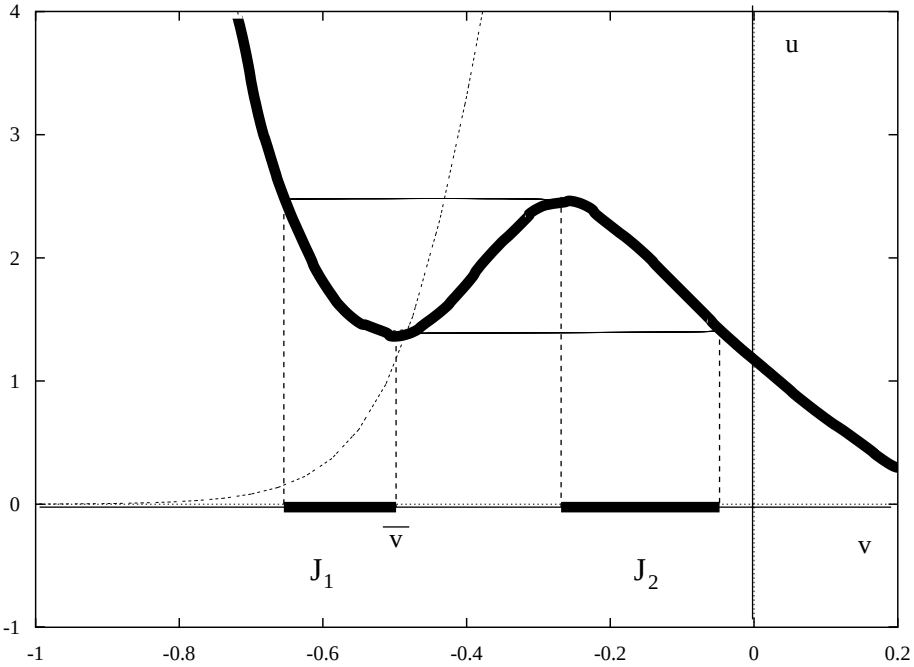

Fig. 11. Effective phase plane of the first oscillator. J_1 and J_2 denote the intervals in v_1 corresponding to the slow segments.

Using (3.40), we rewrite (3.39) as follows:

$$I \equiv \oint_{Z_1(\bar{K})} \frac{c(v_1) f'(v_1)\,\mathrm{d}v_1}{\bar{\omega}(g(v_1) - \tau^{-1}u_1)} + \sum_{i=1}^{s} \oint_{Z_1(\bar{K}_i)} \frac{c(v_1) f'(v_1)\,\mathrm{d}v_1}{\bar{\omega}(g(v_1) - \tau^{-1}u_1)} = 0, \quad \text{where } u_1 = \xi_1 f(v_1) + \bar{K}. \tag{4.41}$$

By J_1 and J_2, we denote the intervals in v, corresponding to the left- and right-hand branches of the slow manifold in the effective phase planes for individual oscillators (see Fig. 11). Since the v-amplitudes of the small oscillations are $\mathrm{O}(\epsilon)$, we rewrite (4.41) as

$$I = I_2 - I_1 + \mathrm{O}(\epsilon), \tag{3.42}$$

where

$$I_i = \int_{J_i} \frac{c(v_1) f'(v_1)\,\mathrm{d}v_1}{\bar{\omega}(g(v_1) - \tau^{-1}u_1)} = 0, \quad u_1 = \xi_1 f(v_1) + \sigma\bar{K}, \quad i = 1, 2.$$

From the definition of $g(v)$, (3.16) and (3.1), we note that

$$g(v) \approx 0 \quad \text{on the most part of } J_1, \qquad g(v) = \mathrm{O}(1) \quad \text{on } J_2.$$

Therefore, $I_1 = \mathrm{O}(\tau) \gg I_2 = \mathrm{O}(1)$, and (3.42) yields

$$\int_{J_1} \frac{c(v_1) f'(v_1)\,\mathrm{d}v_1}{g(v_1) - \tau^{-1}(\xi f(v_1) + K)} \approx 0. \tag{3.43}$$

Because $f(v_1)$ is decreasing on J_1 and $\omega_1 - \omega_2 < 0$, (2.2) implies that $c(v_1)$ is monotonically increasing on J_1. In addition,

$$\frac{f'(v_1)}{g(v_1) - \tau^{-1}(\xi f(v_1) + K)} > 0, \quad v_1 \in J_1.$$

These observations and (3.43) imply that $c(\bar{v}) > 0$. Therefore, near the jump point the second (faster) oscillator moves ahead of the first one. This argument also holds for the mixed-mode limit cycle with more than one large-amplitude oscillations and several small-amplitude oscillations in one period. In our numerical simulations, we find that the second oscillator is dominant for the most part of the family of mixed-mode solutions shown in Fig. 3b. Therefore, the structure of this subfamily of periodic solutions of the continuous system (2.1) and (2.2) is determined by the family of 1D Poincare maps derived for the second oscillator. In particular, Fig. 3b shows the period-adding and the reverse period-adding sequences as predicted by Theorem 3.1.

4. Discussion

Properties of solutions of ordinary differential equations near an AHB have been used to account for many important aspects of neuronal dynamics [1,4,9,14,16,18,19,21–23,26,27,36]. Remarkably, many neural models reside near an AHB. Recent modeling studies of mammalian auditory system suggest that our hearing organ, the cochlea, uses the AHB for tuning and amplification [16,36]. In type II models of excitable cells [47], the AHB bifurcation separates the regions of quiescent and oscillatory behaviors and determines the frequency of the subthreshold oscillations. In [22,23], a mechanism of selective communication via the resonance of the subthreshold oscillations (near an AHB) in a postsynaptic cell with the frequency of bursting of presynaptic cell was demonstrated. Studies of systems of coupled oscillators near an AHB have revealed a number of interesting properties: the phenomenon of quenching of oscillations in chains of intrinsically oscillating elements, the oscillation death [1]; and its counterpart, the oscillations induced by coupling of passive elements [21,29]. In [18,19], the analysis of subcritical Hopf-homoclinic bifurcation was used to explain a spike-frequency adaptation in a model of certain neurons. Recent progress in the geometric theory for singularly perturbed systems [30,31] stimulated applications of canard-related phenomena in models of chemical and biological systems [14,42,48]. The results presented in this paper show that the systems of strongly coupled relaxation oscillators in the regime near an AHB have a large repertoire of oscillatory behavior.

We have studied a system of two coupled oscillators modeling active dendrites of DNs. The model is based on the experimental data [52] and all the parameters are in the physiological range. We had noted that the individual oscillators reside in the regime close to an AHB and investigated the implications of this configuration on the dynamics of the coupled system. We have shown that the coupled system has a rich family of stable multimodal periodic solutions with frequencies and waveforms varying greatly across the family. Using numerical continuation techniques, we have studied the structure and the bifurcations of periodic solutions under variation of the control parameter. The main step in our analysis is the reduction of this problem to the analysis of a family of one-dimensional bimodal maps. In addition to predicting the sequences of different types of stable periodic solutions in the coupled system, which we discussed above, the rescaled Poincare map (3.33) leads to an interesting observation that when the individual oscillators are in less relaxation regime, the coupled system may have notable windows of chaotic behavior. Indeed, for larger values of the relaxation parameter ϵ, the transition between the two outer branches of the map becomes less abrupt (see Fig. 8c), and the appearing middle branch will result in chaotic dynamics for values of τ from certain intervals. We have checked this prediction numerically (not presented in the paper). Except for the procedure of determining of the dominant oscillator (Subsection 3.6), the analysis can be easily

extended to chains with arbitrary number of oscillators. This extension for a closely related problem was done [38]. This suggests that a similar mechanism is responsible for generating of mixed-mode oscillations in large chains of coupled oscillators. Apart from the principle ingredients (such as proximity of the individual oscillators to an AHB, strong electrical coupling, and distributed natural frequencies), the mechanism discussed in this paper is independent on the specific details of the model of the DNs and is relevant for a broader class of chains of two-dimensional relaxation oscillators. Numerically, we have verified existence of similar families of multimodal solutions in chains of modified FitzHugh–Nagumo oscillators [48] and oscillators of Morris–Lecar type [43].

Acknowledgements

We would like to thank N. Kopell for useful conversations. Numerical results presented in this paper were obtained using packages AUTO [13], XPPAUT [17], and MATLAB.

Appendix A. Parameter values

The values of the parameters of (2.1) and (2.2), which we have used in our numerical example, are given in the following table:

E_1	1	c_2	1.4×10^{-2}
E_2	-0.9	c_3	$(1.8)^4$
E_3	-0.5	ϵ	1.3×10^{-2}
$\bar{g}_1$	0.8	τ	10
$\bar{g}_2$	2	d	4.44×10^3
$\bar{g}_3$	1	ω_1	1
c_1	-0.35	ω_2	16

Appendix B. Derivation of the expressions (3.17) and (3.18)

For convenience, we rewrite the effective equations for an individual oscillator (3.14) and (3.15)

$$\frac{\mathrm{d}v}{\mathrm{d}\theta} = \xi f(v) - u + \sigma K, \tag{B.1}$$

$$\frac{\mathrm{d}u}{\mathrm{d}\theta} = \epsilon\omega \frac{g(v) - (1/\tau)u}{a(E_2 - v)}, \tag{B.2}$$

where $\theta = \epsilon^{-1} \int_{t_0}^{t} a(E_2 - v(s))\,\mathrm{d}s$. Note that for $t \geq t_0$ $a(E_2 - v(t)) > 0$ is uniformly bounded from 0.

Let $K = K^0 + \kappa$, where K^0 is the value of K, for which the nullclines intersect at $v = \bar{v}$:

$$K^0 = \sigma(\tau g(\bar{v}) - \xi f(\bar{v})). \tag{B.3}$$

We make a change of variables $w = u - \sigma K^0$ and rewrite (B.1) and (B.2)

$$\frac{\mathrm{d}v}{\mathrm{d}\theta} = \xi f(v) - w, \tag{B.4}$$

$$\frac{\mathrm{d}w}{\mathrm{d}\theta} = \epsilon\omega \frac{g(v) - \sigma\tau^{-1}K^0 - \tau^{-1}w - \sigma\kappa\tau^{-1}}{a(E_2 - v)}. \tag{B.5}$$

In order to apply the results of Krupa and Szmolyan [31], in the neighborhood of $(\bar{v}, \bar{w})$, $\bar{w} = \xi f(\bar{v})$, we transform (B.4) and (B.5) to a normal form by changing variables

$$v = \bar{v} + \alpha V, \qquad w = \bar{w} + \beta W \quad \text{and} \quad \zeta = \gamma\theta,$$

where

$$\alpha = \frac{2\bar{\omega}}{f_2}\sqrt{\frac{g_1\bar{\omega}}{E\omega}}, \qquad \beta = \frac{2\bar{\omega}g_1}{Ef_2}, \qquad \gamma = \sqrt{\frac{E}{\omega g_1}} \quad \text{and} \quad E = a(E_2 - \bar{v}). \tag{B.6}$$

By f_i and g_i, $i = 1, 2, \ldots$, we denote the ith derivatives of f and g, respectively, evaluated at $v = \bar{v}$.

With these choices of α, β, and γ, in the neighborhood of $(\bar{v}, \bar{w})$, (B.4) and (B.5) has the following form:

$$\frac{\mathrm{d}V}{\mathrm{d}\zeta} = -Wh_1 + V^2h_2 + h_3, \tag{B.7}$$

$$\frac{\mathrm{d}W}{\mathrm{d}\zeta} = \epsilon(Vh_4 - \lambda h_5 + Wh_6), \tag{B.8}$$

where $\lambda = (\sigma\gamma\omega/\beta\tau E)\kappa$ and

$$h_1 = 1, \qquad h_2 = 1 + \frac{f_3\alpha}{3f_2}V + \mathrm{O}(V^2), \qquad h_3 = 0, \qquad h_4 = 1 + \frac{g_2\alpha}{2g_1}V + \mathrm{O}(V^2),$$
$$h_5 = 1 + \mathrm{O}(V), \qquad h_6 = \frac{-\omega\gamma}{E\tau}.$$

Following Krupa and Szmolyan [31], we calculate

$$a_1 = \left.\frac{\partial h_3}{\partial V}\right|_0 = 0, \qquad a_2 = \left.\frac{\partial h_1}{\partial V}\right|_0 = 0, \qquad a_3 = \left.\frac{\partial h_2}{\partial V}\right|_0 = \frac{f_3\alpha}{3f_2}, \qquad a_4 = \left.\frac{\partial h_4}{\partial V}\right|_0 = \frac{g_2\alpha}{2g_1},$$
$$a_5 = h_6(0) = \frac{-\omega\gamma}{E\tau}, \qquad A = -a_2 + 3a_3 - 2a_4 - 2a_5 = \frac{2\omega\gamma}{E\tau} + \alpha\left[\frac{f_3}{f_2} - \frac{g_2}{g_3}\right].$$

Note

$$A = \alpha\left(\frac{\xi f_2}{g_1} + \frac{f_3}{f_2} - \frac{g_2}{g_3}\right).$$

The values of λ for the AHB and the canard transition [31]:

$$\lambda^{\mathrm{H}}(\sqrt{\epsilon}) = \frac{\omega\gamma}{2E\tau}\epsilon + \mathrm{O}(\epsilon^{3/2}), \qquad \lambda^{\mathrm{c}}(\sqrt{\epsilon}) = \lambda^{\mathrm{H}} - \frac{1}{8}A\epsilon + \mathrm{O}(\epsilon^{3/2}).$$

Therefore,

$$\kappa^{\mathrm{H}} = \frac{\sigma E\tau\beta}{\omega\gamma}\lambda^{\mathrm{H}} = \frac{\sigma\beta}{2}\epsilon + \mathrm{O}(\epsilon^{3/2}), \qquad \kappa^{\mathrm{c}} = \sigma\left\{\frac{\beta}{4} - \frac{\alpha\beta\tau E}{\gamma\omega}\left[\frac{f_3}{f_2} - \frac{g_2}{g_1}\right]\right\}\epsilon + \mathrm{O}(\epsilon^{3/2}).$$

By noting $\beta = \alpha/\gamma$, we have

$$\kappa^{\mathrm{c}} = \sigma\left\{\frac{\beta}{4} - \frac{\beta^2\tau E}{\omega}\left[\frac{f_3}{f_2} - \frac{g_2}{g_1}\right]\right\}\epsilon + \mathrm{O}(\epsilon^{3/2}).$$

Appendix C. Proof of Theorem 3.1

First, we find the regions of existence for cycles p^1, $p \in \mathbb{N}$. Let $\{x_i : x_{i+1} = P_\lambda(x_i), i = 1, 2, 3, \dots\}$ be the semiorbit starting at $\lambda - 1 \le x_1 \le 0$. Periodic orbit p^1 exists iff

$$P_{\lambda,r} P^p_{\lambda,l}(x_1) = x_1 \quad \text{for some } x_1 \in [\lambda - 1, 0], \tag{C.1}$$

provided $P^{p-1}_{\lambda,l}(x_1) \le 0$. Note that (C.1) is a linear equation in x_1. It always has a real solution. This solution generates a cycle p^1 if $x_1 \in [\lambda - 1, 0]$. Therefore, we have to consider two cases:

(a) $x_1 = \lambda - 1$ (the orbit passing through the lower knee of (3.33)),
(b) $x_1 = 0$ (the orbit passing through the upper knee of (3.33)).

- Case (a):

$$\begin{aligned} &x_1 = \lambda - 1,\\ &x_2 = l(\lambda - 1) + \lambda,\\ &\cdots\\ &x_{p+1} = \underbrace{l(\cdots(l(l}_{p}(\lambda - 1) + \lambda) +) \cdots + \lambda) + \lambda\\ &= l^p(\lambda - 1) + \lambda(1 + l + l^2 + \cdots + l^{p-1})\\ &= l^p(\lambda - 1) + \lambda\frac{1 - l^p}{1 - l}. \end{aligned}$$

  By requiring $x_{p+1} = 0 + 0$, we obtain

$$\underline{\lambda}(p) = \frac{l^p(1 - l)}{1 - l^{p+1}}.$$

- Case (b): Let $x_1 = r\lambda + \lambda - 1 < 0$. Then

$$x_p = P^{p-1}_{\lambda,l}(x_1) = l^{p-1}(\lambda(r + 1) - 1) + \lambda(1 + l + l^2 + \cdots + l^{p-2}) = l^{p-1}\lambda(r + 1) + \lambda\frac{1 - l^p}{1 - l}.$$

  By requiring $x_p = 0$, we obtain

$$\bar{\lambda}(p) = \frac{l^{p-1}(1 - l)}{1 - l^p + rl^{p-1}(1 - l)}.$$

Thus, we have proved (3.34).

Next, we verify relations (3.36):

$$\begin{aligned} \underline{\lambda}(p) - \bar{\lambda}(p) &= \frac{l^p(1 - l)}{1 - l^{p+1}} - \frac{l^{p-1}(1 - l)}{1 - l^p + rl^{p-1}(1 - l)} = \frac{l^{p-1}(1 - l)(l + rl^p(1 - l) - 1)}{(1 - l^{p+1})(1 - l^p + rl^{p-1}(1 - l))}\\ &< \frac{l^{p-1}(1 - l)(l + (1 - l) - 1)}{(1 - l^{p+1})(1 - l^p + rl^{p-1}(1 - l))} = 0, \end{aligned} \tag{C.2}$$

$$\underline{\lambda}(p) - \underline{\lambda}(p + 1) = \frac{l^p(1 - l)}{1 - l^{p+1}} - \frac{l^{p+1}(1 - l)}{1 - l^{p+2}} = \frac{l^p(1 - l)^2}{(1 - l^{p+1})(1 - l^{p+2})} > 0, \tag{C.3}$$

$$\bar{\lambda}(p + 1) = \frac{l^p(1 - l)}{1 - l^{p+1} + rl^p(1 - l)} < \frac{l^p(1 - l)}{1 - l^{p+1}} = \underline{\lambda}(p). \tag{C.4}$$

The inequalities (3.36) follow from (C.2) and (C.3).

To prove (3.35) and (3.37), we note that the families of cycles 1^p and p^1 and their regions of existence are symmetric with respect to the transformations:

$$l \mapsto r, \qquad r \mapsto l, \qquad \underline{\lambda} \mapsto 1 - \bar{\mu}, \qquad \bar{\lambda} \mapsto 1 - \underline{\mu}.$$

References

[1] D.G. Aronson, G.B. Ermentrout, N. Kopell, Amplitude response of coupled oscillators, Physica D 41 (1990) 403–449.
[2] S.M. Baer, T. Erneux, Singular Hopf bifurcation to relaxation oscillations, SIAM J. Appl. Math. 46 (1986) 721–739.
[3] S.M. Baer, T. Erneux, Singular Hopf bifurcation to relaxation oscillations, II, SIAM J. Appl. Math. 52 (1992) 1651–1664.
[4] S.M. Baer, T. Erneux, J. Rinzel, The slow passage through a Hopf bifurcation: delay, memory effects, and resonance, SIAM J. Appl. Math. 49 (1989) 55–71.
[5] E. Benoit, J.L. Callot, F. Dienner, M. Dienner, Chasse au canard, Collect. Math. 32 (1981) 37–119.
[6] N.N. Bogoliubov, Yu.A. Mitropolsky, Asymptotic Methods in the Theory of Non-linear Oscillations, Hidustan Publishing Corp., Delhi, 1961.
[7] F. Buchholtz, M. Dolnik, I. Epstein, Diffusion-induced instabilities near a canard, J. Phys. Chem. 99 (1995) 15093–15101.
[8] J.L. Callot, F. Diener, M. Diener, Le probleme de la chasse au canard, C.R. Acad. Sci. Paris, Ser. I 286 (1978) 1059–1061.
[9] Y. Choe, M.O. Magnasco, A.J. Hudspeth, A model for amplification of hair-bundle motion by cyclical binding of Ca^{2+} to mechanoelectrical-transduction channels, PNAS USA 95 (1998) 15321–15326.
[10] P. Dayan, L.F. Abbot, Theoretical Neuroscience: Computational and Mathematical Theory of Neural Systems, MIT Press, Cambridge, MA, 2001.
[11] M. Diener, The Canard unchained or how fast/slow dynamical systems bifurcate, Math. Intellect. 6 (1984) 38–49.
[12] E.J. Ding, P.C. Hemmer, Exact treatment of mode locking for a piecewise linear map, J. Statist. Phys. 46 (1987) 99–110.
[13] E. Doedel, A.R. Champneys, T.F. Fairgrieve, Yu.A. Kuznetsov, B. Sandstede, X.J. Wang, AUTO 97: continuation and bifurcation software for ordinary differential equations, 1997. http://cmvl.cs.concordia.ca/publications.html.
[14] J. Drover, J. Rubin, J. Su, B. Ermentrout, Analysis of a canard mechanism by which excitatory synaptic coupling can synchronize neurons at low firing frequencies, Preprint.
[15] W. Echhaus, Relaxation oscillations including a standard chase on French ducks, in: Lecture Notes in Mathematics, vol. 985, 1983, pp. 449–497.
[16] V.M. Eguiluz, et al., Essential nonlinearities in hearing, Phys. Rev. Lett. 84 (22) (2000) 5232–5235.
[17] B. Ermentrout, Simulating, Analyzing, and Animating Dynamical Systems: A Guide to XPPAUT for Researches and Students, SIAM, Philadelphia, 2002.
[18] J. Guckenheimer, R. Harris-Warrick, J. Peck, A. Willms, Bifurcation, bursting, and spike-frequency adaptation, J. Comp. Neurosci. 4 (1997) 257–277.
[19] J. Guckenheimer, A. Willms, Asymptotic analysis of subcritical Hopf-homoclinic bifurcation, Physica D 139 (1997) 195–216.
[20] J. Guckenheimer, P. Holmes, Nonlinear Oscillations, Dynamical Systems, and Bifurcations of Vector Fields, Springer, 1983.
[21] F.C. Hoppensteadt, E.M. Izhikevich, Synaptic organizations and dynamical properties of weakly connected neural oscillators, Biol. Cybernet. 75 (1996) 117–127.
[22] E.M. Izhikevich, Resonance and selective communication via burst in neurons having subthreshold oscillations, BioSystems 67 (2002) 95–102.
[23] E.M. Izhikevich, N.S. Desai, E.C. Walcot, F.C. Hoppensteadt, Bursts as a unit of neural information: selective communication via resonance, Trends Neurosci. 26 (2003) 161–167.
[24] C.K.R.T. Jones, Geometric singular perturbation theory, in: CIME Lectures in Dynamical Systems, Lecture Notes in Mathematics, Springer-Verlag, 1994.
[25] J.P. Keener, Chaotic behavior in piecewise continuous difference equations, Trans. AMS 261 (1980) 589–604.
[26] J.P. Keener, J. Rinzel, Hopf bifurcation to repetitive activity in nerve, SIAM J. Appl. Math. 43 (1983) 907–922.
[27] N. Kopell, G.B. Ermentrout, Mechanisms of phase-locking and frequency control in pairs of coupled neural oscillators, in: B. Fiedler (Ed.), Handbook of Dynamical Systems, Elsevier, Amsterdam, 2002, pp. 3–54.
[28] M.T.M. Koper, Bifurcations of mixed-mode oscillations in a three-variable autonomous van der Pol–Duffing model with a cross-shaped phase diagram, Phys. D 80 (1995) 72–94.
[29] J.M. Kowalski, G.L. Albert, B.K. Roades, G.W. Gross, Neuronal networks with spontaneous, correlated bursting activity: theory and simulations, Neural Networks 5 (1992) 805–822.
[30] M. Krupa, P. Szmolyan, Extending geometric singular perturbation theory to nonhyperbolic points. Folds and canard points in two dimensions, SIAM J. Math. Anal. 33 (2001) 286–314.
[31] M. Krupa, P. Szmolyan, Relaxation oscillation and canard explosion, JDE 174 (2001) 312–368.
[32] A.Yu. Kuznetsov, Elements of Applied Bifurcation Theory, Springer, 1998.

[33] M. Levi, A period-adding phenomenon, SIAM J. Appl. Math. 50 (4) (1990) 943–955.
[34] T. LoFaro, A period-adding bifurcations in a one parameter family of interval maps, Math. Comput. Model. 24 (1996) 27–41.
[35] T. LoFaro, N. Kopell, Timing regulation in a network reduced from voltage-gated equations to a one-dimensional map, J. Math. Biol. 38 (1999) 479–533.
[36] M.O. Magnasco, A wave traveling over Hopf instability shapes cochlear tuning curve, Phys. Rev. Lett. 90 (5) (2003) 58101–58104.
[37] Yu.L. Maistrenko, V.L. Maistrenko, S.I. Vikul, On period-adding sequences of attracting cycles in piecewise linear maps, Chaos, Solitons, and Fractals 9 (1998) 67–75.
[38] G.S. Medvedev, N. Kopell, Synchronization and transient dynamics in the chains of electrically coupled FitzHugh–Nagumo oscillators, SIAM J. Appl. Math. 61 (2001) 1762–1801.
[39] G.S. Medvedev, C.J. Wilson, J.C. Callaway, N. Kopell, Dendritic synchrony and transient dynamics in a coupled oscillator model of the dopaminergic neuron, J. Comp. Neurosci. 15 (1) (2003) 53–69.
[40] A. Milik, P. Szmolyan, H. Løffelman, E. Grøller, Geometry of mixed-mode oscillations in the 3D autocatalator, Int. J. Bifurc. Chaos 8 (1998) 505–519.
[41] E.F. Mishchenko, Yu.S. Kolesov, A.Yu. Kolesov, N.Kh. Rozov, Asymptotic Methods in Singularly Perturbed Systems, Consultants Bureau, New York, 1994.
[42] J. Moehlis, Canards in a surface oxidation reaction, J. Nonlin. Sci. 12 (2002) 319–345.
[43] C. Morris, H. Lecar, Voltage oscillations in the barnacle giant muscle fiber, Biophys. J. 35 (1981) 193–213.
[44] J. Nagumo, S. Sato, On a response characteristic of a mathematical neuron model, Kybernetik 3 (1972) 155–164.
[45] V. Petrov, S.K. Scott, K. Showalter, Mixed-mode oscillations in chemical systems, J. Chem. Phys. 97 (9) (1992) 6191–6198.
[46] J. Ringland, N. Issa, M. Schell, From U sequence to Farey sequence: a unification of one parameter scenarios, Phys. Rev. A 41 (8) (1990) 4223–4235.
[47] J. Rinzel, G.B. Ermentrout, Analysis of neural excitability and oscillations, in: C. Koch, I. Segev (Eds.), Methods in Neuronal Modeling, MIT Press, Cambridge, MA, 1989.
[48] H.G. Rotstein, N. Kopell, A.M. Zhabotinsky, I.R. Epstein, Localization in systems of equivalent relaxation type oscillators with global inhibitory coupling: a canard mechanism, SIAM J. Appl. Math. 63, 1098–2019.
[49] W. Singer, Time as coding space, Curr. Opin. Neurobiol. 9 (1999) 189–194.
[50] E.I. Volkov, D.V. Volkov, Multirhythmicity generated by slow variable diffusion in a ring of relaxation oscillators and noise-induced abnormal interspike variability, Phys. Rev. E 65 (2002).
[51] P. Waelti, A. Dickson, W. Schultz, Dopamine responses comply with basic assumptions of formal learning theory, Nature 421 (5) (2001) 43–48.
[52] C.J. Wilson, J.C. Callaway, A coupled oscillator model of the dopaminergic neuron of the substantia nigra, J. Neurophysiol. 83 (2000) 3084–3100.
[53] S. Yoshizava, H. Osada, J. Nagumo, Pulse sequences generated by a degenerate analog neuron model, Biol. Cybernet. 45 (1982).